International Journal of Plasticity xxx (xxxx) xxx–xxx

Contents lists available at ScienceDirect

International Journal of Plasticity

journal homepage: www.elsevier.com/locate/ijplas

Transgranular amorphous shear band formation in polycrystalline boron carbide

Dezhou Guo, Qi An*

Department of Chemical and Materials Engineering, University of Nevada-Reno, Reno, NV, 89557, United States

ARTICLE INFO

Keywords:
Nanoceramics
Boron carbide
Grain boundaries
DFT
ReaxFF
Intragranular failure

ABSTRACT

Intragranular failure plays an important role in the failure process of superhard nanocrystalline ceramics. But the atomistic deformation mechanisms leading to intragranular failure have not been well established. Here we performed large-scale reactive force field (ReaxFF) reactive molecular dynamics (RMD) simulations on the finite shear deformation of nanocrystalline boron carbide (n-B_4C) with a grain size of 9.74 nm. We find that intragranular amorphization initiates from grain boundaries (GBs) and propagates along the rhombohedral (011) < $2\bar{1}\bar{1}$> slip system. To illustrate the atomic mechanism of amorphous shear band formation along this slip system, we combined density functional theory (DFT) and RMD simulations on the shear deformation of single crystal B_4C. These simulations displayed that the dislocation nucleation occurs along this slip system, accompanied with bond breaking of intraicosahedral bonds within $B_{11}C$ cage. This leads to the amorphous shear band formation under the applied shear deformation. Our simulations suggest that the coupling of dislocation nucleation and GB sliding leads to the intragranular amorphous shear band formation and may leads to the intragranular failure in n-B_4C.

1. Introduction

The Hall-Petch relationship describes the grain boundary (GB) strengthening phenomena that the GBs act as barriers to block the mobile dislocation, leading to an increased yield strength as the grain size decreases (Schiøtz et al., 1998). However, a reverse Hall-Petch relationship would be expected when grain size is reduced below a critical value in which dislocations can break through the GBs and move freely (Schiøtz and Jacobsen, 2003). For nanocrystalline metals, the intragranular deformation primarily occurs in the Hall-Petch relationship region while the intergranular deformation mainly initiates in the reverse Hall-Petch relationship region (Shimokawa et al., 2005). This is because stress concentrates near the GBs in larger grain size due to the pile-up of dislocations, facilitating the activation of intragranular deformation within grains. However, in smaller grain size, GB sliding which involves small atomic scale GB migration could easily occur to accommodate the geometrical misfits, accelerating the intergranular deformation. The resistances of intergranular and intragranular deformation are influenced by external conditions. Particularly, Coble creep dominates in the intergranular deformation under high temperature and low applied stress, but superplasticity by grain boundary sliding is prevalent under a high strain rate and moderate temperature. For nanocrystalline ceramics, although both conventional and breakdown of Hall-Petch relationships have been observed recently (Ryou et al., 2018), it has not been well established how the intragranular or intergranular deformation depends on grain-size and external conditions (e.g., temperature, pressure and strain rate).

In recent years, the atomistic processes of deformation mechanism in nanocrystalline metals are extensively investigated (Latapie

* Corresponding author.
E-mail address: qia@unr.edu (Q. An).

https://doi.org/10.1016/j.ijplas.2019.06.004
Received 22 March 2019; Received in revised form 14 May 2019; Accepted 8 June 2019

and Farkas, 2004; Inoue et al., 1995; Shimokawa et al., 2005; Xu et al., 2016; Tong et al., 2016; Cao et al., 2018; Lu et al., 2019; Prakash et al., 2017; Bieler et al., 2009). Molecular dynamics (MD) simulations (Shimokawa et al., 2005; Latapie and Farkas, 2004; Inoue et al., 1995) have been employed to investigate the intergranular deformation caused by GB sliding and grain rotation accommodation, as well as the intragranular deformation induced by crystal slips and pile-up dislocations. The underlying atomic mechanisms of these studies are of great helpful to achieve high strength, yet ductile metals and ceramics through GB engineering. Although the intergranular deformation mechanism was observed to be dominated in nanocrystalline boron carbide (Guo et al., 2018), it is essential to investigate the intragranular deformation behaviors in ceramics since it is the dominate deformation modes in many ceramics (Luo et al., 2018; Alan et al., 2010; Niihara et al., 1994; Wang et al., 2003). In addition, for superhard ceramics, the local amorphization provides a specialty of structure destruction under deformation (Chen et al., 2003), which is different from metal alloys where the mobile dislocations are dominated in deformation and failure processes.

To illustrate the atomistic mechanism controlling the deformation and fracture of polycrystalline superhard ceramics, we used boron carbide (B_4C) as a prototype material because of such excellent mechanical properties as high hardness, high Hugoniot elastic limit (HEL) and low density. These excellent properties arise from the unique structural characteristics of B_4C, which consists of 12-atom icosahedra couple with three-atom C–B–C chains to form a rhombohedral unit cell in which the icosahedra are roughly cubic closest packed (Bourne, 2002; Sezer and Brand, 2001; Thévenot, 1990; Domnich et al., 2011; Mauri et al., 2001; Xie et al., 2016). Despite its hardness, B_4C displays abnormal shear strength reduction under high pressures, limiting its widespread engineering applications (Grady, 1998; Ghosh et al., 2012; Holmquist and Johnson, 2006). Previous hypervelocity impact, scratch, and indentation experiments revealed that amorphous shear band formation is the dominant deformation and failure mode of B_4C resulting in shear softening and brittle failure (Chen et al., 2003; Fujita et al., 2014; Reddy et al., 2013). We have recently explained the origin of the amorphous shear band formation and its role in the brittle failure by combining:

- density function theory (DFT) simulations on B_4C single crystal show that amorphous shear bands initiate because shear deformation causes the C–B–C chain react with the broken C–B bond between icosahedra to disintegrate the icosahedra (An et al., 2014).
- reactive molecular dynamics (RMD) simulations on periodic cells with length scales of 25 nm (~200,000 atoms) show that the abnormal brittle failure arises because disintegrated icosahedra in amorphous shear bands increase the density, leading to local tensile stresses that induce cavitation that results in crack opening (An and Goddard, 2015).

Recently, we further examined how GBs affect the mechanical response of nanocrystalline boron carbide (n-B_4C) (Guo et al., 2018). We found that GB sliding is the dominate deformation mechanism in n-B_4C in which the shear prefers to align the GBs, deconstructing icosahedra. We did not consider the void effects in n-B_4C, which may play an important role in the intragranular fracture in micro size B_4C. In this Article, to illustrate the intragranular amorphization mechanism in n-B_4C, we applied the combination of ReaxFF reactive molecular dynamics (RMD) and density functional theory (DFT) simulations to investigate the finite shear deformation of n-B_4C and single crystal B_4C. We found that the intraicosahedral bond breaking leads to the initiation of intragranular amorphous shear band formation, which propagates along the rhombohedral $(011) < 2\bar{1}\bar{1}>$ slip system. The deformation mechanism along this particular slip system indicates a dislocation nucleation induced amorphous shear band formation. Our results suggest that the intragranular failure in B_4C may arise from the intragranular amorphous shear bands formation due to the dislocation nucleation.

2. Simulation methods

2.1. Grain boundary model in MD simulations

The system examined herein is the GB model of n-B_4C with the grain size of 9.74 nm containing 1,092,685 atoms. The structure is constructed by the Voronoi construction approach: first, the seeds associated with various rotation matrixes are inserted in the supercell; then, each grain around the seed is cut out by the Voronoi polygon; finally, 16 randomly oriented grains are pasted together into a BCC lattice to form the polycrystalline model shown in Fig. 1. To equilibrate the GB model, we first minimize the structure at 0 K, followed by an annealing process from 1000 K to room temperature within 500 ps using the NPT ensemble (constant pressure, constant temperature, and constant number of atoms). Then we carried out NPT RMD simulations at room temperature until the internal stresses of system were relaxed to zero. The equilibrium density at ambient condition from ReaxFF is $\rho_0 = 2.58\ \mathrm{g\,cm^{-3}}$, in good agreement with the experimental value of $2.52\ \mathrm{g\,cm^{-3}}$ at 300 K.

To quantify the local plastic deformation during the shear process, we computed the Von-Mises shear strain n_i^{Mises} for each atom (Shimizu et al., 2007). This measure was incorporated into visualization program AtomEye (Li, 2003). The calculation of n_i^{Mises} requires two atomic configurations: the sheared configuration, and the initial referent configuration. A local transformation matrix J_i are sought which best maps

$$\{\boldsymbol{d}_{ji}^0\} \rightarrow \{\boldsymbol{d}_{ji}\},\ \forall\, j \in N_i^0 \tag{1}$$

where d's are vector separations between atom j and i (superscript 0 means the referent configuration). j is one of atom i's nearest neighbors, and N_i^0 is the total number of nearest neighbors of atom i, at the reference configuration. J_i is determined by minimizing

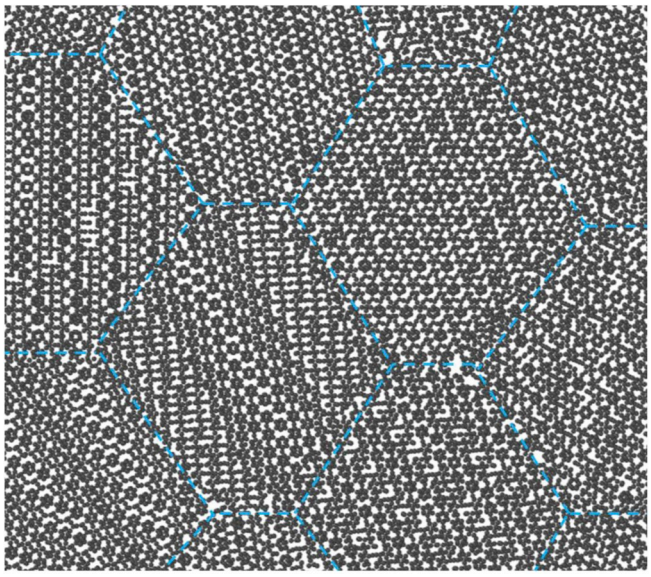

Fig. 1. The simulation model of nanocrystalline B_4C with 9.74 nm grain size (1,092,685 atoms). It consists of 16 randomly oriented grains arranged on the BCC lattice. The dotted blue lines represent the grain boundaries. (For interpretation of the references to color in this figure legend, the reader is referred to the Web version of this article.)

$$\sum_{j\in N_i^0} |\boldsymbol{d}_{ji}^0 \boldsymbol{J}_i - \boldsymbol{d}_{ji}|^2 \rightarrow \boldsymbol{J}_i \left(\sum_{j\in N_i^0} \boldsymbol{d}_{ji}^{0T} \boldsymbol{d}_{ji}^0 \right)^{-1} \left(\sum_{j\in N_i^0} \boldsymbol{d}_{ji}^{0T} \boldsymbol{d}_{ji}^0 \right) \tag{2}$$

For each J_i, the local Lagrangian strain matrix is computed as

$$n_i = \frac{1}{2}(J_i J_i^T - I) \tag{3}$$

Then atom i's local shear invariant can be computed as

$$\boldsymbol{n}_i^{Mises} = \sqrt{n_{yz}^2 + n_{yz}^2 + n_{yz}^2 + \frac{(n_{yy} - n_{zz})^2 + (n_{xx} - n_{zz})^2 + (n_{xx} - n_{yy})^2}{6}} \tag{4}$$

2.2. RMD simulations

To perform RMD simulations, we used the ReaxFF reactive force field incorporated into the large-scale atomic/molecular massively parallel simulator (LAMMPS) software (Plimpton, 1995). In structure minimization, the potential energy and geometries are optimized by adjusting the atomic positions and cell parameters. Then we carried out isothermal–isobaric (NPT) RMD simulations to achieve an equilibrated state at ambient condition with the Nose–Hoover thermostat and barostat. The 100 fs damping constant and 1000 fs damping constant were applied for controlling the temperature and pressure, respectively in NPT dynamics. The periodic boundary conditions were applied along all three directions and the integration time step was set to 0.25 fs

After the equilibrium structure was obtained, we applied shear deformation to examine the mechanical responses since shear is the dominated deformation modes leading to amorphous shear band formation in B_4C (An et al., 2014). We sheared the system along $x-z$ plane until failure at a constant shear rate of 0.1 ps^{-1} with the NVT ensemble (constant volume, constant temperature, and constant number of atoms). The damping constant for Nose–Hoover thermostat is 100 fs in NVT RMD simulations.

2.3. DFT simulations

DFT simulations were performed by the Vienna Ab-initio Simulation Package (VASP) periodic code with plane wave basis sets (Kresse and Hafner, 1993, 1996). We used an energy cutoff of 500 eV for the plane wave expansions. The Perdew-Burke-Ernzerh (PBE) functional and the projector augmented-wave (PAW) method are applied for the exchange-correlation interaction and the core-valence interaction, respectively (Paier et al., 2005; Kresse and Joubert, 1999). The pseudopotentials in PAW method consider the $2s^2 2p^2$ electrons and $2s^2 2p^1$ electrons as valence states for C and B elements, respectively. The energy error for terminating electronic self-consistent field and the force criterion for the geometry optimization were set equal to 1×10^{-5} eV and 1×10^{-2} eV·Å^{-1}, respectively. The Brillouin zone integration was performed on Γ-centered symmetry reduced Monkhorst−Pack meshes with a fine resolution of $2\pi \times 1/40$ Å^{-1}.

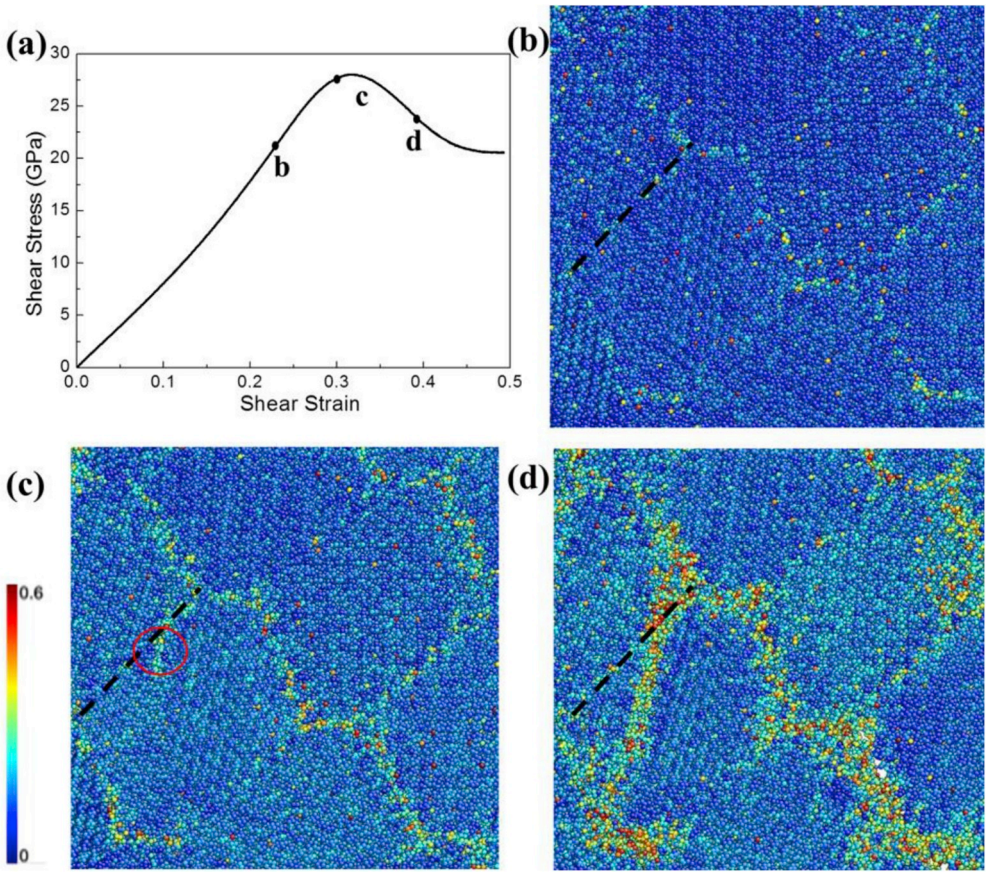

Fig. 2. (a) The shear-stress – shear-strain relationship of GB model during the finite shear deformation with a 0.1/ps strain rate. (b–d) Atomic configurations for GB models at various shear strains: (b) Elastic deformation at 0.23 shear strain, the majority of deformation occurs at GB regions; (c) Initiation of intragranular atomic sliding at 0.3 shear strain; (d) Intragranular and intergranular amorphization at 0.375 shear strain. The color coding is based on the atomic shear strain. The dotted lines represent the original GB position. (For interpretation of the references to color in this figure legend, the reader is referred to the Web version of this article.)

In order to obtain the failure mechanism of B_4C especially under complex stress conditions, we examined the deformation behaviors as a function of the pure shear strain and biaxial shear strain that mimics a complex indenter loading environment. For pure shear deformation, we applied shear strain along a particular slip system while relaxing the structure to minimize the other five stress components (Roundy et al., 1999). The biaxial shear deformation is used to imitate the compressed condition with a biaxial stress distribution with a shear stress σ_{xz} and a normal compressive stress component σ_{zz}, following the equation of $\sigma_{zz} = \sigma_{xz}\tan\varphi$, where $\varphi = 68^\circ$ (Li et al., 2014). The biaxial shear deformation is to mimic the complex stress conditions of indentation experiments.

3. Results and discussion

3.1. Deformation mechanism of GB model

Fig. 2a exhibits the shear-stress – shear-strain relationships of the GB model during shear deformation at a strain rate of 0.1/ps. In order to illustrate the detailed deformation mechanism during shear process, we selected several critical snapshots to display the critical events leading to failure. At first, the continuously linear increase in shear stress τ from 0 to 0.275 shear strain illustrates a unitary elastic deformation without any significant local plastic deformation, as shown in Fig. 2b. Then, a short plastic deformation process occurs, suggested by a decreased slope in the shear-stress – shear-strain curve from 0.275 to 0.325 shear strain, gradually reaching to the maximum yield stress of 28.01 GPa. Here, since most of relative movements of atoms accumulate within GB regions, we expect that GBs sliding is the prevalent deformation mechanism during shear process, leading to the amorphization at these easily fracture crossover regions where pre-distorted icosahedra exist. However, instead of intergranular GBs sliding, an obvious atomic sliding region initiates from one GB and orients towards internal grain at 0.3 shear strain, as shown in the oval in Fig. 2c. The GB facilitates the activation of intragranular sliding propagation which leads to an amorphous band formation and further developing into shear band with ~2 nm in width (Fig. 2d).

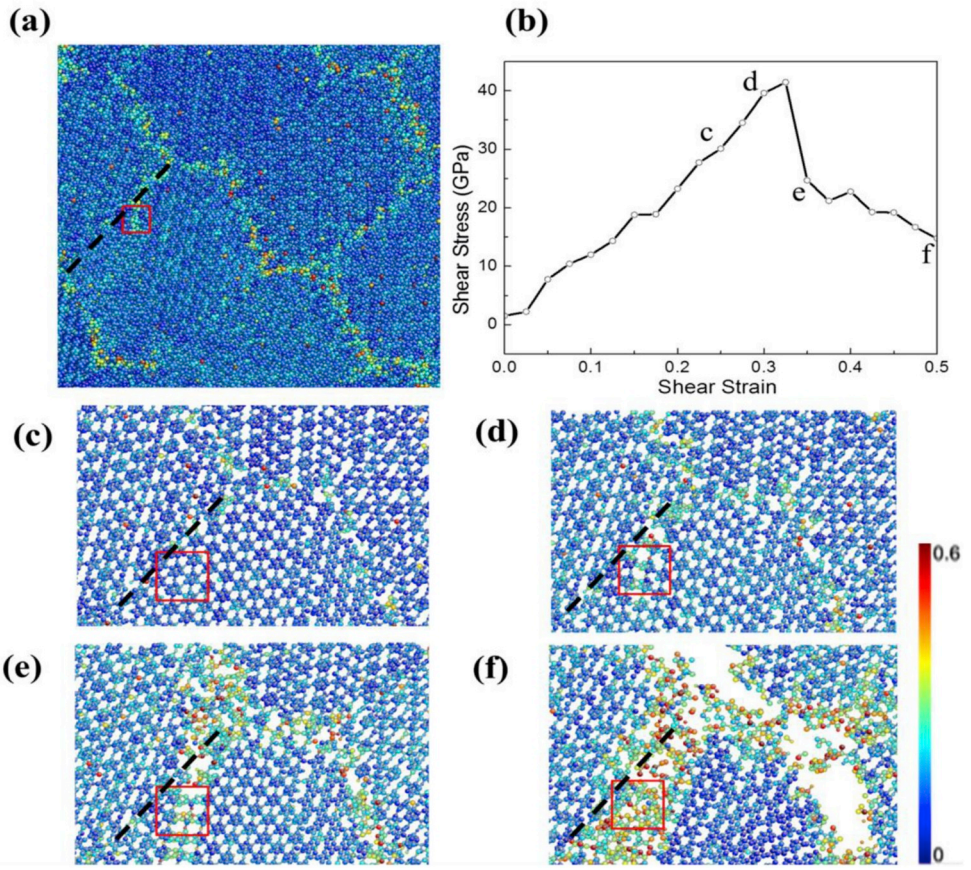

Fig. 3. (a) Snapshots of atomic configuration at 0.3 shear strain. An 1 nm × 1 nm × 1 nm cube in the initiated intragranular deformation region (as shown in red square) near GB was selected. (b) Shear-stress – shear-strain relations of the selected region. (c–f) Snapshots of GB sliding at 0.25 shear strain, initiated intragranular atom sliding at 0.3 shear strain, bond breakings at 0.35 shear strain and amorphization at 0.5 shear strain. Only the first layer of icosahedra is displayed for better illustration. The color coding is based on the atomic shear strain. The dotted lines represent the original GB position. (For interpretation of the references to color in this figure legend, the reader is referred to the Web version of this article.)

3.2. Local deformation mechanism of intragranular deformation

The local stress state and the specific slip system could be two possible reasons to cause intragranular deformation mode alternative to GB sliding. In order to analyze the essential local state evolution of the amorphous shear band formation within the grain, we drew the shear stress as a function of shear strain (Fig. 3b) by selecting a 1 nm × 1 nm × 1 nm cube at the initiated grain sliding spot (Fig. 3a). Also, we extracted snapshots of critical states to analyze the local deformation process.

- The continuous increase in shear stress τ from initial structure to 0.3 shear strain illustrates a uniformly elastic deformation. During this process, the GB sliding is the dominant deformation mechanism. For example, no visually relative atomic movements can be found in the selected area at 0.25 strain, but a handful of GB sliding do exist in the GB regions, as shown in Fig. 3c.
- The GB sliding transforms to intragranular sliding at 0.3 shear strain. As the shear strain increases to 0.325, the local shear stress reaches the maximum value of 41.5 GPa, which is higher than the maximum shear strength of the whole system (Fig. 3a). This is due to the stress localization in the granular region, leading to local bond breaking.
- The sharp drop of the shear stress arises from the deconstruction of icosahedral clusters which cause amorphous shear band formations within the grain, releasing regional stresses (Fig. 3e).
- As shear strain continuously increases, the further amorphization significantly relieve the shear stress to 14.74 GPa at 0.5 shear strain (Fig. 3f). The cavitation occurs in the highly amorphization GB region, leading to the failure of the whole structure.

3.3. Deformation mechanism along (011) < 2$\bar{1}\bar{1}$> *slip system*

Here, our RMD simulation results indicate that the intragranular fracture occurs along the (011) < 2$\bar{1}\bar{1}$> slip system. Therefore, it is essential to understand the deformation and failure mechanism along this particular slip system.

In order to understand the how the detailed deformation mechanism at this specific gliding system of (011) < 2$\bar{1}\bar{1}$>, we carried out

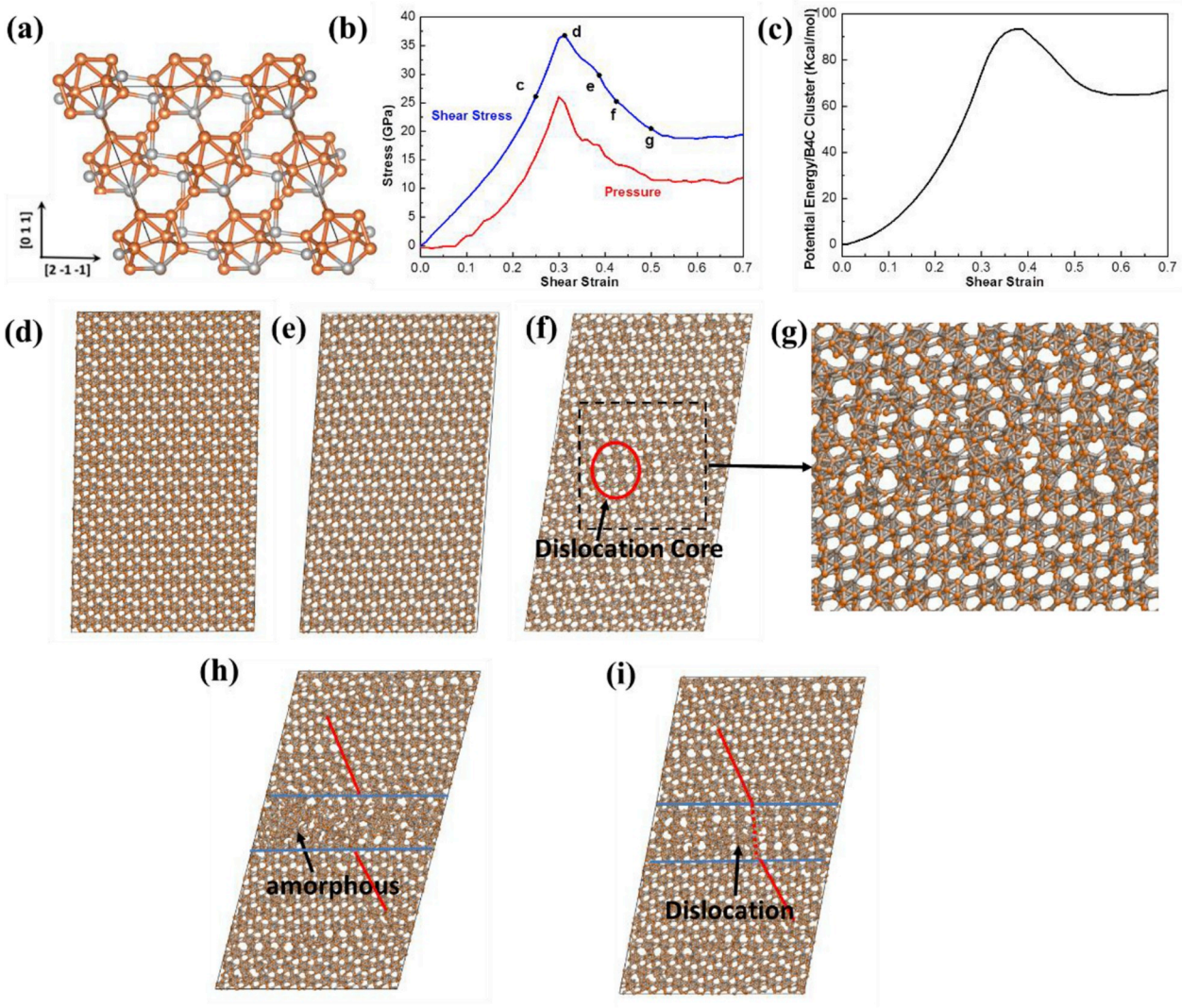

Fig. 4. The initial unit cell, shear-stress − shear-strain relations and some critical snapshots for shear along slip system (011) < 2$\bar{1}\bar{1}$>, showing the successive process of amorphous band formation. (a) The unit structural model of B_4C showing the slip system. (b) The shear stress and pressure are plotted to show the shear strain dependence. (c) The potential energy is plotted to show the shear strain dependence. (d–i) Snapshots of shearing showing the successive processes of dislocation and amorphous band formation: (d) intact structure. (e) structure at 0.31 shear strain corresponding to the maximum shear stress; (f) structure at 0.39 shear strain corresponding to the maximum potential energy and a dislocation nucleation; (g) magnified structure showing the dislocation region; (h) structure at 0.425 shear strain corresponding to the dislocation expansion with stress relaxation; and (i) structure at 0.5 shear strain amorphous band (~1.5 nm in width) formation.

the finite shear RMD simulation on the shear deformation along (011) < 2$\bar{1}\bar{1}$> slip system. Here, for computational convenience, the structure is rotated to the direction that x − z plane is the (011) slip plane and x-axis is along the <2$\bar{1}\bar{1}$> slip direction in a Cartesian coordinate system, as shown in Fig. 4a. To have a clearly insight of the amorphous band formation process, we construct a supercell containing 21,600 atoms with the cell dimensions of $a = 5.82$ nm, $b = 10.33$ nm, and $c = 2.80$ nm through expanding the unit cell by $6 \times 12 \times 5$ times for each dimension. The equilibrium density from ReaxFF is $\rho_0 = 2.56\ \mathrm{g\,cm^{-3}}$, in good agreement with the experimental value of $2.52\ \mathrm{g\,cm^{-3}}$ at 300 K. It is interesting to notice that our ReaxFF predicted a lower density in perfect crystal than that of above GB model. This is because that the amorphous phase along GBs is slightly higher in density than crystal phase (An and Goddard, 2015). The supercell is sheared along x − z plane until failure to examine the mechanical response.

The following steps are observed during the deformation process:

- First, the continuous increase of the shear stress τ and total pressure P until reaching the maximum value of $\tau = 36.8$ GPa and $P = 26.0$ GPa at 0.31 shear strain indicates an elastic deformation, as displayed in Fig. 4d and e. There are no visible changes of atomic positions in addition to the lattice distortion.
- Next, the plastic deformation initiates, resulting in a quick drop in τ and P. When the shear strain increases to 0.39, a dislocation

initiates with the Burgers vector of $\frac{1}{4}[2\bar{1}\bar{1}]$(Fig. 4f) leading to a slightly reduced slope of the shear-stress – shear-strain relationship. Meanwhile, the potential energy reaches to its maximum value.

- Then, a ~2 nm wide dislocation zone is formed at 0.425 shear strain (Fig. 4g) accompanying with intraicosahedral bonds breaking within icosahedra.
- Finally, an amorphous shear band forms and develops into ~2 nm zone at 0.5 strain, as shown in Fig. 4i. This amorphous bond initiates around the dislocation core, where the B_4C icosahedra intensively deformed due to the severe straining caused by dislocation motion. Amorphous band formation dramatically relieves the total pressure from 14.2 to 11.6 GPa and the shear stress from 26.7 to 22 GPa.

3.4. Bond breaking process for dislocation initiation from DFT simulations

Our above RMD simulation shows that the bond breaking plays a significant role in dislocation and amorphous shear band nucleation. However, in our GB model, the stress conditions of intragranular dislocation formation are complex due to the local stress concentration in nearby GB regions. Thus, in order to understand the detailed atomistic bond breaking processes resulting in the initial destructions of icosahedral cluster during shear process, we applied both pure shear QM simulations and biaxial shear deformation to investigate failure mechanisms along $(011) < 2\bar{1}\bar{1}>$ slip system. The shear stress-strain relationship is displayed in Fig. 5(a1 and a2) and several critical snapshots of bond breaking processes are displayed in Fig. 5(b1-d1 and b2-d2).

For the pure shear simulation, the system deforms elastically to 0.254 strain, then turns into plastic deformation as the slope of stress-strain curve gradually reduces. the shear stress reaches the maximum value of 44.67 GPa at 0.345 strain before failure starts. Due to the larger ideal shear strength, The $(011) < 2\bar{1}\bar{1}>$ slip system is harder to active compared to $(001) < 100>$ slip system and $(111) < 2\bar{1}\bar{1}>$ slip system, which are two most plausible activated slip systems for B_4C (Yang et al., 2018). However, this slip system may be activated in n-B4C because of local stress concentration, as we observed in above RMD simulations.

A similar stress-strain evolution applies to the biaxial shear deformation. An elastic deformation from 0 to 0.187 strain follows with a plastic deformation process until 0.209 strain until at which the maximum shear stress of 31.52 GPa is achieved. For both cases, the icosahedra are not deconstructed as the shear stress reaches its maximum.

As the shear strain increases, bonds stretch continuously and bonds breakings between three boron atoms from two icosahedra are observed both in pure shear and biaxial shear systems. For pure shear situation, the bond between B_1 and B_2 boron atoms were stretched to 2.03 Å at 0.368 strain, leading to a 1.22 GPa drop of shear stress; when the shear strain comes to 0.392, the distance of B_1–B_2 boron atomsis stretched to 2.60 Å, indicating the ruptures of this bond, which is responsible for the destruction of the icosahedron and failure of the whole system with the shear stress sharply decreases to 27.40 GPa. For biaxial shear case, the initial B_1–B_2 bond stretching following by its breaking at 0.254 strain are the reasons of the whole system failure.

4. Conclusions

In summary, Our RMD simulations indicate that the deformation mechanism of the superhard n-B_4C is not only the GB sliding, but also intragranular amorphous band formation. Our RMD and DFT simulations provide a detailed atomic mechanism revealing the formation of intragranular dislocation and amorphization in n-B4C. This mechanism will be useful for design polycrystal superhard ceramics. Our major findings are:

(1) GB sliding is the prevalent deformation mechanism of n-B_4C, but intragranular failure might initiate from GBs and propagate at specific slip system, such as$(011) < 2\bar{1}\bar{1}>$ slip system.
(2) The intragranular failure nucleates from GBs at plastic deformation period before reaching to the yield strength.
(3) In the specific $(011) < 2\bar{1}\bar{1}>$ slip system for perfect crystal, amorphous band formation initiates around dislocation core where the icosahedra intensively deformed and develops into amorphous zones.
(4) Intraicosahedral bonds breaking within icosahedra plays a significant role in dislocation formation, amorphous band formation and structure failure.

Our results may provide useful information for GB engineering to tune the fracture modes in superhard ceramics. Although GB sliding is the dominant deformation mechanism for nanocrystalline ceramics, intragranular sliding, dislocation and amorphous shear band formation could be expected when easily activated slip systems were activated along GB. These findings also stress the significance of nanostructure in the materials' properties and may illustrate a new way to design ductile ceramics with improved mechanical properties.

Competing interests

The authors declare no competing financial interests.

Acknowledgements

This work is supported by the U.S. Nuclear Regulatory Commission (NRC-HQ-84-15-G-0028) and NSF (CMMI-1727428).

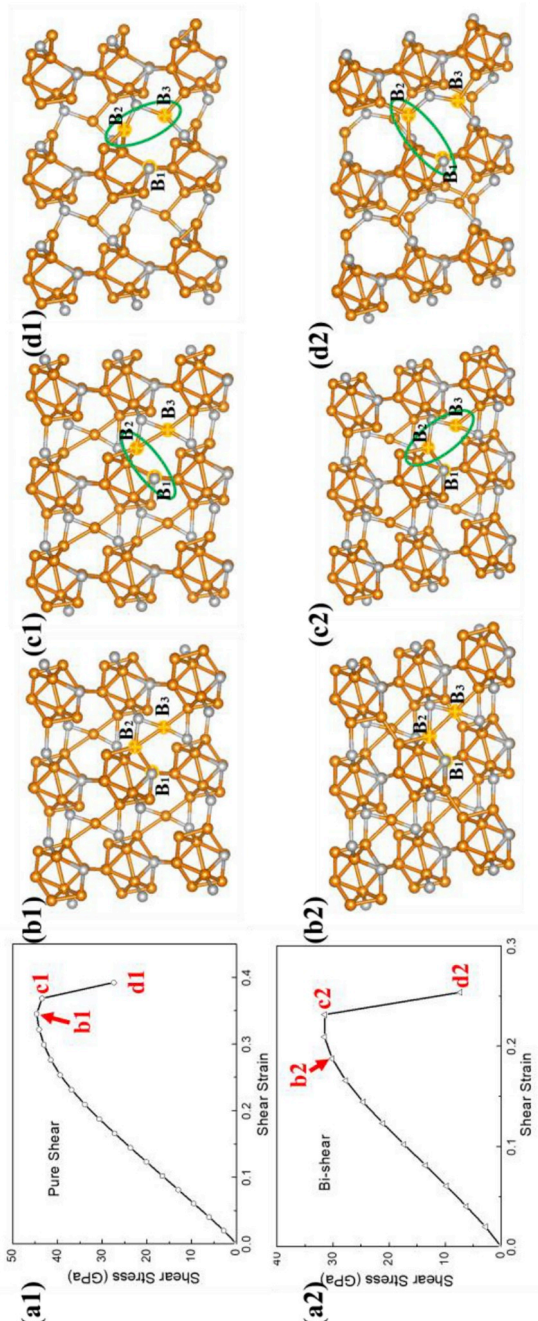

Fig. 5. The shear-stress–shear-strain relationship of n-B_4C along (011) < $2\bar{1}\bar{1}$> slip system under (a1) pure shear deformation; (a2) bi-shear deformation. (b1, b2) Intact structure; (c1, c2) structures with B_1-B_2 bond obvious stretched structure; (d1, d2) failed structure with deconstructed icosahedra.

Appendix A. Supplementary data

Supplementary data to this article can be found online at https://doi.org/10.1016/j.ijplas.2019.06.004.

References

Alan, P., Sang-Ho, L., Messing, G.L., 2010. Processing and microstructure development in alumina-silicon carbide intragranular particulate composites. J. Am. Ceram. Soc. 77, 2157–2164.
An, Q., Goddard III, W.A., 2015. Atomistic origin of brittle failure of boron carbide from large-scale reactive dynamics simulations: suggestions toward improved ductility. Phys. Rev. Lett. 115, 105501.
An, Q., Goddard III, W.A., Cheng, T., 2014. Atomistic explanation of shear-induced amorphous band formation in boron carbide. Phys. Rev. Lett. 113, 095501.
Bieler, T.R., Eisenlohr, P., Roters, F., Kumar, D., Mason, D.E., Crimp, M.A., Raabe, D., 2009. The role of heterogeneous deformation on damage nucleation at grain boundaries in single phase metals. Int. J. Plast. 25, 1655–1683.
Bourne, N.K., 2002. Shock–induced brittle failure of boron carbide. Proc. Roy. Soc. Lond. A 458, 1999–2006.
Cao, Z.H., Sun, W., Yang, X.B., Zhao, J.W., Ma, Y.J., Meng, X.K., 2018. Intersectant coherent twin boundaries governed strong strain ardening behavior in nano-crystalline Cu. Int. J. Plast. 103, 81–94.
Chen, M., McCauley, J.W., Hemker, K.J., 2003. Shock-induced localized amorphization in boron carbide. Science 299, 1563–1566.
Domnich, V., Reynaud, S., Haber, R.A., Chhowalla, M., 2011. Boron carbide: structure, properties and stability under stress. J. Am. Ceram. Soc. 94, 3605–3628.
Fujita, T., Guan, P., Reddy, K.M., Hirata, A., Guo, J., Chen, M., 2014. Asymmetric twins in rhombohedral boron carbide. Appl. Phys. Lett. 104, 021907.
Ghosh, D., Subhash, G., Zheng, J.Q., Halls, V., 2012. Influence of stress state and strain rate on structural amorphization in boron carbide. J. Appl. Phys. 111, 063523.
Grady, D.E., 1998. Shock-wave compression of brittle solids. Mech. Mater. 29, 181–203.
Guo, D., Song, S., Luo, R., Goddard III, W.A., Chen, M., Reddy, K.M., An, Q., 2018. Grain boundary sliding and amorphization are responsible for the reverse Hall-Petch relation in superhard nanocrystalline boron carbide. Phys. Rev. Lett. 121, 145504.
Holmquist, T.J., Johnson, G.R., 2006. Characterization and evaluation of boron carbide for plate-impact conditions. J. Appl. Phys. 100, 093525.
Inoue, H., Akahoshi, Y., Harada, S., 1995. Molecular dynamics simulation on fracture mechanisms of nano-scale polycrystal under static and cyclic loading. Mater. Sci. Res. Int. 1, 95–99.
Kresse, G., Furthmüller, J., 1996. Efficiency of ab-Initio total energy calculations for metals and semiconductors using a plane-wave basis set. Comput. Mater. Sci. 6, 15–50.
Kresse, G., Hafner, J., 1993. Ab initio molecular dynamics for liquid metals. Phys. Rev. B 47, 558–561.
Kresse, G., Joubert, D., 1999. From ultrasoft pseudopotentials to the projector augmented-wave method. Phys. Rev. B 59, 1758–1775.
Latapie, A., Farkas, D., 2004. Molecular dynamics investigation of the fracture behavior of nanocrystalline α-Fe. Phys. Rev. B 69, 134110.
Li, J., 2003. AtomEye: an efficient atomistic configuration viewer. Model. Simul. Mater. Sci. Eng. 11, 173–177.
Li, B., Sun, H., Chen, C., 2014. Large indentation strain-stiffening in nanotwinned cubic boron nitride. Nat. Commun. 5, 4965.
Lu, X.C., Zhang, X., Shi, M.X., Roters, F., Kang, G.Z., Raabe, D., 2019. Dislocation mechanism based size-dependent crystal plasticity modeling and simulation of gradient nano-grained copper. Int. J. Plast. 113, 52–73.
Luo, J.T., Luo, S.Y., Zhang, C.X., Xue, Y.H., Chen, G.Q., 2018. Analysis of the intragranular microstructure in ceramic nanocomposites and their effect on the mechanical properties. J. Am. Ceram. Soc. 101, 5151–5156.
Mauri, F., Vast, N., Pickard, C.J., 2001. Atomic structure of icosahedral B_4C boron carbide from a first principles analysis of NMR spectra. Phys. Rev. Lett. 87, 085506.
Niihara, K., Ünal, N., Nakahira, A., 1994. Mechanical properties of (YTZP)-alumina-silicon carbide nanocomposites and the phase stability of Y-TZP particles in it. J. Mater. Sci. 29, 164–168.
Paier, J., Hirschl, R., Marsman, M., Kresse, G., 2005. The Perdew-Burke-Ernzerhof Exchange-Correlation functional applied to the G2-1 test set using a plane-wave basis set. J. Chem. Phys. 122, 234102.
Plimpton, S., 1995. Fast parallel algorithms for short-range molecular dynamics. J. Comput. Phys. 117, 1–19.
Prakash, A., Weygand, D., Bitzek, E., 2017. Influence of grain boundary structure and topology on the plastic deformation of nanocrystalline aluminum as studied by atomistic simulations. Int. J. Plast. 97, 107–125.
Reddy, K.M., Liu, P., Hirata, A., Fujita, T., Chen, M.W., 2013. Atomic structure of amorphous shear bands in boron carbide. Nat. Commun. 4, 2483.
Roundy, D., Krenn, C., Cohen, M., Morris, J., 1999. Ideal shear strengths of Fcc aluminum and copper. Phys. Rev. Lett. 82, 2713–2716.
Ryou, H., Drazin, J.W., Wahl, K.J., Qadri, S.B., Gorzkowski, E.P., Feigelson, B.N., Wollmershauser, J.A., 2018. Below the Hall−Petch limit in nanocrystalline ceramics. ACS Nano 12, 3083–3094.
Schiøtz, J., Jacobsen, K.W., 2003. A maximum in the strength of nanocrystalline copper. Science 301, 1357–1359.
Schiøtz, J., Di Tolla, F.D., Jacobsen, K.W., 1998. Softening of nanocrystalline metals at very small grain sizes. Nature 391, 561–563.
Sezer, A.O., Brand, J.I., 2001. Chemical vapor deposition of boron carbide. Mater. Sci. Eng. B 79, 191–202.
Shimizu, F., Ogata, S., Li, J., 2007. Theory of shear banding in metallic glasses and molecular dynamics calculations. Mater. Trans. 48, 2923–2927.
Shimokawa, T., Nakatani, A., Kitagawa, H., 2005. Grain-size dependence of the relationship between intergranular and intragranular deformation of nanocrystalline Al by molecular dynamics simulations. Phys. Rev. B 71, 224110.
Thévenot, F., 1990. Boron carbide—a comprehensive review. J. Eur. Ceram. Soc. 6, 205–225.
Tong, X., Wang, G., Yi, J., Ren, J.L., Pauly, S., Gao, Y.L., Zhai, Q.J., Mattern, N., Dahmen, K.A., Liaw, P.K., Echert, J., 2016. Shear avalanches in plastic deformation of metallic glass composite. Int. J. Plast. 77, 141–155.
Wang, X., Shan, Y., Yu, X., Xu, J., Yin, Y.S., Zhou, Y., 2003. Formation and mechanism of intragranular structure in zirconia-toughened alumina ceramics with nano-ZrO_2 and micro-Al_2O_3. J. Chin. Ceram. Soc. 31, 1145–1149.
Xie, K.Y., An, Q., Sato, T., Breen, A.J., Ringer, S.P., Goddard III, W.A., Cairney, J.M., Hemker, K.J., 2016. Breaking the icosahedra in boron carbide. Proc. Natl. Acad. Sci. Unit. States Am. 113, 12012–12016.
Xu, X., Wang, Y., Guo, A., Geng, H., Ren, S., Tao, X., Liu, J., 2016. Enhanced plasticity by nanocrystallite in bulk amorphous Al_2O_3-ZrO_2-Y_2O_3. Int. J. Plast. 79, 314–327.
Yang, X.K., Coleman, S.P., Lasalvia, J.C., Goddard III, W.A., An, Q., 2018. Shear-induced Brittle Failure along Grain Boundaries in Boron Carbide, vol. 10. pp. 5072–5080.